Icarus 224 (2013) 201–208

Contents lists available at SciVerse ScienceDirect

Icarus

journal homepage: www.elsevier.com/locate/icarus

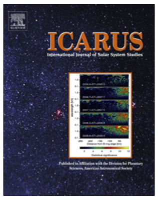

Probing the inner boundaries of Saturn's A ring with the Iapetus $-1{:}0$ nodal bending wave

Matthew S. Tiscareno [a,*], Matthew M. Hedman [a], Joseph A. Burns [a,b], John W. Weiss [c,d], Carolyn C. Porco [c]

[a] *Department of Astronomy, Cornell University, Ithaca, NY 14853, USA*
[b] *College of Engineering, Cornell University, Ithaca, NY 14853, USA*
[c] *CICLOPS, Space Science Institute, 4750 Walnut Street, Boulder, CO 80301, USA*
[d] *Physics and Astronomy Department, Carleton College, 1 North College Street, Northfield, MN 55057, USA*

ARTICLE INFO

Article history:
Received 21 December 2012
Revised 22 February 2013
Accepted 22 February 2013
Available online 6 March 2013

Keywords:
Planetary rings
Resonances, Rings
Saturn, Rings

ABSTRACT

The Iapetus $-1{:}0$ nodal bending wave, the first spiral wave ever described in Saturn's rings, has been seen again for the first time in 29 years. We demonstrate that it is in fact the nodal bending wave, not the 1:0 apsidal density wave as previously reported. We use wavelet analysis to determine the wavelength profile, thus deriving the surface density at every point in the region covered by the bending wave. This profile is consistent with surface densities measured from more localized spiral density waves in the outer Cassini Division and the inner and mid-A Ring, varying smoothly from the low values of the former to the higher values of the latter.

Most remarkably, our analysis indicates that there is no significant change in surface density across the boundary between the outer Cassini Division and the inner-A ring, despite the very abrupt increase in optical depth and reflected brightness at this location. We consider anew the nature of the classically identified "inner edge of the A ring," given that it does not appear to be correlated with any abrupt increase in surface density. There is an abrupt increase in surface density at the Pandora 5:4 density wave, ~300 km outward of the A ring's inner edge. Further study is needed to robustly interpret our findings in terms of particle properties and abundances, much less to explain the origins of the implied structure.

1. Introduction

Spiral density waves and spiral bending waves, generated in a disk by resonant interactions with perturbing moons, are a pervasive and useful feature in Saturn's rings (see, e.g., Tiscareno, 2013). The very first spiral wave ever reported in Saturn's rings, confirming the prediction of Goldreich and Tremaine (1978, 1979, 1980) that the spiral phenomena well-known in galaxies should also appear in planetary rings, was described by Cuzzi et al. (1981) from *Voyager* 1 imaging data and identified as the Iapetus 1:0 apsidal density wave. The long-wavelength Iapetus wave was the only one resolvable in the comparatively low-resolution *Voyager* 1 images, which were the first available rings data as release of the *Voyager* 1 RSS radio occultation data was delayed (Tyler et al., 1983) and the PPS stellar occultation was not carried out until *Voyager* 2 (Esposito et al., 1983).

Eventually, a panoply of density and bending waves were observed in the *Voyager* RSS and PPS data sets (see references in Tiscareno et al., 2007), but curiously, the Iapetus wave described by Cuzzi et al. (1981) was never seen again by *Voyager*. Similarly, when *Cassini* imaging and occultations revealed a new level of finer-scale spiral waves (see references in Colwell et al., 2009b), the Iapetus wave still was not seen.

We report here that the long-lost Iapetus wave was pointed out for the first time in 29 years in *Cassini* images taken during 2009. As when *Voyager* 1 discovered this wave, Saturn was close to equinox at the time the wave was recovered. The *Voyager* 1 flyby of 1980 November 12 was eight months after the 1980 March 3 equinox, and similarly, the Iapetus wave is most prominent in images taken within about a year of the 2009 August 11 equinox. By contrast, it is very difficult to see in images taken closer to *Cassini*'s 2004 arrival at Saturn, as well as in the most recent images from 2012. Around equinox, the edge-on approach of incident sunlight to the rings (Fig. 1) highlighted vertical structure of many kinds, including radial corrugations (Hedman et al., 2011), impact ejecta clouds (Tiscareno et al., 2013), vertically scalloped gap edges (Weiss et al., 2009; Spitale and Porco, 2010), shadows cast by "propellers" and other compact embedded structures (Tiscareno et al.,

---

* Corresponding author.
E-mail address: matthewt@astro.cornell.edu (M.S. Tiscareno).

0019-1035/$ - see front matter © 2013 Elsevier Inc. All rights reserved.
http://dx.doi.org/10.1016/j.icarus.2013.02.026

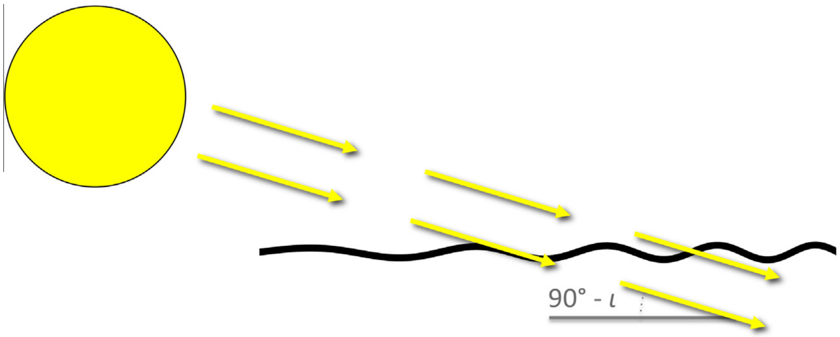

Fig. 1. In this cartoon, the corrugation of the ring by a bending wave, seen edge-on, is represented by the black line. The yellow circle represents the Sun, and the yellow arrows represent the path of sunlight. The complement of the solar incidence angle ι is marked in gray. When the Sun is low on the horizon (i.e., ι is near 90°) sunlight passes through at a shallower angle in some regions of the wave than in others (represented by the lower and upper ray paths, respectively), leading to a modulation in the measured slant optical depth that corresponds with the corrugations. This effect is only seen near local noon or midnight; by contrast, at local morning and evening, sunlight passes along the peaks and troughs (into or out of the page, in this representation) rather than across them. For purposes of readability, the wave amplitude is exaggerated in this cartoon; there is no evidence that slopes in the Iapetus nodal bending wave are ever as large as the angle of incident sunlight (cf. Gresh et al., 1986; Rosen and Lissauer, 1988), even during equinox, when the angular size of the Sun enforces a minimum value for the latter.

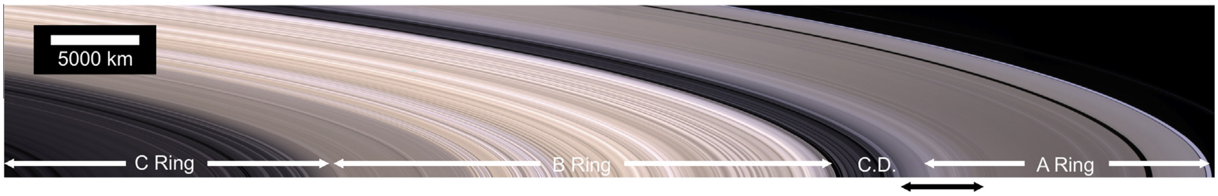

Fig. 2. An overview of Saturn's main rings, with the primary regions marked. The Cassini Division (marked "C.D.") is between the A and B rings. Along the bottom edge of the image, the black double-headed arrow indicates the region of interest for this work, which is shown in more detail in Fig. 3.

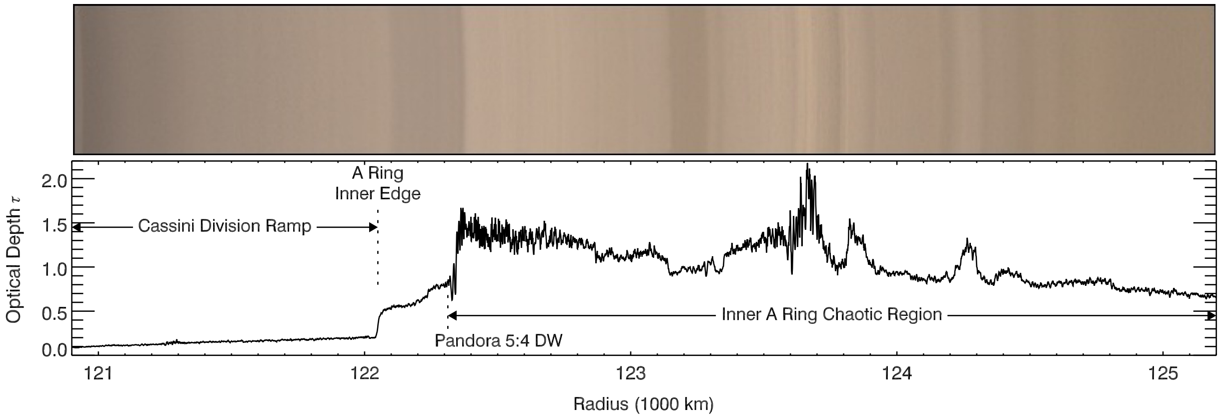

Fig. 3. The region of interest for this work (see Fig. 2 for larger context) consists of the outer Cassini Division and the inner A ring. The bottom panel shows the optical depth τ for the region as measured by a *Cassini* VIMS stellar occultation (tracking the attenuation of the star γ Crucis as *Cassini* saw it pass behind the rings on 2008 October 16). The top panel is an image mosaic taken 2008 November 26, showing a fairly typical (non-equinox) view of the region, with apparent brightness correlating with the optical depth structure.

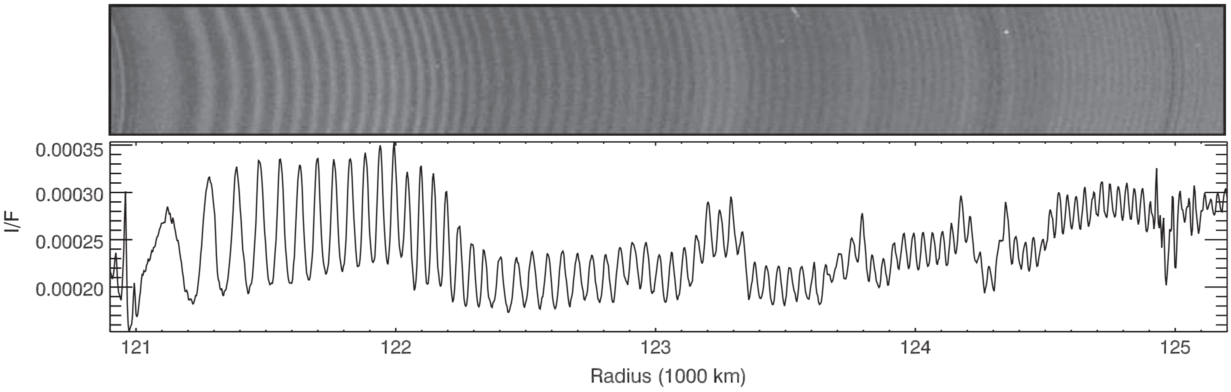

Fig. 4. The same region shown in Fig. 3 as seen during equinox, with the optical depth structure greatly muted and the Iapetus nodal bending wave dominant. The upper panel is an image mosaic taken 2009 August 10, while the lower panel is a radial brightness profile of the same mosaic.

2010a; Spitale and Porco, 2010), and shadows cast on the rings by moons.[1] The association with equinox, along with our detailed analysis of the wavetrain itself (see Section 5), confirm the long-standing suspicion that Cuzzi et al. (1981) saw not the Iapetus 1:0 apsidal density wave, but rather the vertically corrugated Iapetus $-1{:}0$ nodal bending wave (see Section 3).

After an overview of the spatial context of the wave in the next section, we give detailed comments on the nature of resonances and spiral waves in Section 3. Then we describe our observations in Section 4 and our wavelet analysis of the Iapetus nodal bending wave in Section 5. Discussion of our results and their implications for the outer Cassini Division and inner A ring is contained in Section 6.

2. Spatial context

The two most prominent components of Saturn's ring system are the A ring and the B ring. They are separated by the Cassini Division, named for its 17th-century discoverer, which turns out to be a multifaceted ring region in its own right, similar in character to the inner and equally tenuous C ring (Fig. 2). Surface densities in the main part of the Cassini Division are 1–3 $\mathrm{g\,cm^{-2}}$ (Tiscareno et al., 2007; Colwell et al., 2009a), much lower than the characteristic values of 40 $\mathrm{g\,cm^{-2}}$ for the A ring (e.g., Tiscareno et al., 2007) and the even higher values characteristic of the B ring (Robbins et al., 2010).

The outermost part of the Cassini Division is the "Ramp," so called because both the optical depth τ and the apparent brightness[2] I/F in this region increase gradually with ring radius from the low values of the main part of the Cassini Division, reaching relatively higher values at the inner edge of the A ring, at which both parameters then jump to much higher values (Fig. 3). Infrared spectroscopy indicates that the composition of material in the Ramp has more in common with the A ring than it does with the main part of the Cassini Division (Hedman et al., 2013). A very similar Ramp marks the outermost regions of the C ring, with τ and I/F rising with ring radius toward the inner edge of the B ring (Colwell et al., 2009b).

The inner edge of the A ring is traditionally marked at a sharp jump in both τ and I/F occurring at 122,050 km from Saturn's center (Fig. 3; see also French et al., 1993). It has heretofore been presumed that there is a correspondingly sharp jump in surface density σ at the same location, as that is the most straightforward explanation for a higher τ. Although there is no clear reason why there should be a boundary of any kind at this location,[3] it was suggested by Durisen et al. (1992) that, once formed, any boundary would be sharpened via ballistic transport due to bombardment of the ring by interplanetary meteoroids.

A few hundred km outward of the A ring's inner edge is a second sharp jump in both τ and I/F, this one at the location of the Pandora 5:4 Lindblad resonance at 122,313 km, which drives a strong density wave. Outward of this resonant location is a region several thousand km in annular width, characterized by seemingly chaotic radial structure (Fig. 3) that may be due to viscous overstability (Thomson et al., 2007; Hedman et al., 2012; Rein and Latter, 2013), a process by which an over-active restoring force causes small perturbations in density to grow into concentric radial structure with wavelengths $\sim$100 m (Schmidt et al., 2009). The Janus/Epimetheus 4:3 resonance at $\sim$125,250 km marks the outer boundary of the chaotic/overstable region, beyond which is the relatively quiescent mid-A ring.

As shown in Fig. 4, the appearance of this region is greatly altered in the equinox images. The optical depth structure that usually dominates the apparent brightness (Fig. 3) is greatly washed out due to the edge-on illumination, and the apparent brightness is instead dominated by a quasi-periodic pattern generated by the vertical corrugation of the bending wave (illustrated in Fig. 1).

3. Resonances and spiral waves

3.1. General introduction

Spiral waves (Goldreich and Tremaine, 1982; Shu, 1984) occur in planetary rings at locations of resonance between an external forcing frequency, usually a moon's mean motion n' (that is, its average angular velocity), and the natural orbital frequencies of ring particles. The most widespread understood structure in Saturn's rings are *spiral density waves* (see Tiscareno et al., 2007, and references therein), in which the eccentricities of ring particles on resonant orbits are pumped up, leading to a compression wave in which both particle motions and wave propagation are radial.[4] Also significant are *spiral bending waves* (see, e.g., Shu et al., 1983), in which it is the inclinations of resonant ring particles that are pumped up, leading to a transverse wave that also propagates radially but with particle motions in the vertical direction.

Spiral waves occur at locations where the ring particle mean motion n is near an integer ratio (such as 3:2, 5:3, or 10:9) with the perturbing moon's mean motion n'. This is formally expressed in terms of the resonance argument φ, which librates about a constant value (i.e., $\dot{\varphi} \approx 0$) for particles in the resonance. The most prominent class of resonances in Saturn's rings are first-order (i.e., the two integers differ only by one), with the rings interior to the perturbing moon. For a spiral density wave of this type, $\dot{\varphi}$ is of the form

$$\dot{\varphi}_{\mathrm{DW}} = mn' - (m-1)n - \dot{\varpi}, \tag{1}$$

where m is an integer identifying[5] the $m{:}\,(m-1)$ resonance, and $\dot{\varpi}$ is the ring particle's apsidal precession rate.[6] The resonance argument for spiral bending waves is similar, but with the ring particle's nodal precession rate $\dot{\Omega}$ instead of $\dot{\varpi}$. The precession rates are nonzero because Saturn's asphericity, whose effect on the gravity field is described to first order by the parameter J_2, causes a ring particle's radial and vertical frequencies to differ from its mean motion (see, e.g., Murray and Dermott, 1999). However, there is an unusual class of spiral waves for which n does not appear in the relevant equations; these are driven by commensurability between the perturbing moon's mean motion and the ring particle's precession alone.

The simplest of these is an *apsidal density wave*, driven by a simple commensurability between the perturber's mean motion n' and the ring particle's apsidal precession rate $\dot{\varpi}$, which is to say that the long axis of the ring particle's elliptical orbit points toward the perturbing moon.[7] The resonance argument is simply

---

[1] See images PIA11498, PIA11506, PIA11634, PIA11651, and PIA11660 at `http://photojournal.jpl.nasa.gov`.

[2] I/F is a measure of observed brightness normalized by the incident solar flux density.

[3] One recent suggestion is that the Mimas 2:1 resonance, which now forms the outer edge of the B ring (inner edge of the Cassini Division) was once at this location, and that subsequent inward orbital migration of Mimas excavated what is now the Cassini Division (Lainey et al. (2012a,b)).

[4] Particle motions are also excited in the azimuthal direction for both types of waves, which partly defines the waves' spiral structure; and, of course, the unexcited (keplerian) particle motions are azimuthal.

[5] m is also the number of spiral arms in the resulting density/bending wave.

[6] The line of apsides is the long axis of an orbital ellipse, assuming non-zero eccentricity; thus, *apsidal precession* is the angular motion of the orbital ellipse within the orbit plane. The line of nodes is the line of intersection between the orbit plane and the reference plane, when the inclination is non-zero; thus, *nodal precession* is the angular motion of the orbit plane.

[7] This is identical to the *evection resonance* that appears in the dynamics of Earth's Moon and other satellites, in that case with the Sun playing the part of the perturber.

$$\dot{\varphi}_{\mathrm{ADW}} = n' - \dot{\varpi}, \tag{2}$$

which naturally leads to the resonance being labeled "1:0," after the respective integer coefficients of n' and n, with reference to Eq. (1). A similar commensurability involving n' and the ring particle nodal precession rate $\dot{\Omega}$ leads to the *nodal bending wave* (Rosen and Lissauer, 1988), in which it is the ring particle's orbit plane that precesses in time with the perturber's mean motion. However, for an oblate planet such as Saturn, nodes precess "backwards" (i.e. $\dot{\Omega} < 0$); thus,[8] the simplest argument that constitutes a valid resonance is

$$\dot{\varphi}_{\mathrm{NBW}} = -n' + \dot{\varpi}' + \dot{\Omega}' - \dot{\Omega}. \tag{3}$$

While interpreting Eq. (3), keep in mind that the middle two terms are very small compared to the outer two, since apsidal and nodal resonances involve perturbing moons that are so far from the planet that their orbital rates are comparable to the precession rates of ring particle orbits, but that both $\dot{\Omega}$ and $\dot{\Omega}'$ are negative. Again following (one might say *ad absurdam*) the system for labeling resonances and their spiral waves based on the integer coefficients of n' and n, the nodal resonance is labeled "−1:0."

Because of the "backwardness" inherent in the nodal resonance, nodal bending waves propagate radially outward (when the perturber is outward of the rings, as is the case for all resonances discussed in this work) as do density waves, rather than inward as do other bending waves. Furthermore, because the frequencies involved with apsidal and nodal resonances are much lower than for other wave-producing resonances (due to the absence of the ring particle's mean motion in $\dot{\varphi}$), their waves have much longer wavelengths than typical spiral waves and are excited by moons orbiting much farther from Saturn. Indeed, while typical spiral waves are excited by the inner moons Pan, Atlas, Prometheus, Pandora, Janus, Epimetheus, and Mimas, the only known moons whose apsidal and nodal resonances fall within the main rings are Titan, Hyperion, and Iapetus. Of these, Titan's apsidal resonance governs an eccentric ringlet in the mid-C ring (Porco et al., 1984; Nicholson and Porco, 1988) while its nodal bending wave is nearby (Rosen and Lissauer, 1988), Hyperion's waves are weak but have been seen in the mid-C ring and will be discussed in another publication by M.S. Tiscareno and B.E. Harris (in preparation), and Iapetus' waves are the subject of this work.

3.2. Dispersion relations and wavenumber profiles

Because their low amplitudes fall far short of saturating the background, all spiral waves considered in this work follow the linear theory (Goldreich and Tremaine, 1982; Shu, 1984), relevant parts of which we now reproduce. Mindful of some variations among authors, we largely follow the notation of Rosen et al. (1991), as Tiscareno et al. (2007) did with more comment.

The dispersion relation for an apsidal spiral density wave is

$$[n' - n(r)]^2 = [n(r) - \dot{\varpi}(r)]^2 - 2\pi G\sigma_{\mathrm{b}}|k(r)|, \tag{4}$$

where G is Newton's constant, σ_{b} is the background surface density, and n and $\dot{\varpi}$ and the wavenumber $k = 2\pi/\lambda$ (where λ is the spatial wavelength) are functions of the radial location r. Similarly, the dispersion relation for a nodal spiral bending wave is

$$[-n' + \dot{\varpi}' + \dot{\Omega}' - n(r)]^2 = [n(r) - \dot{\Omega}(r)]^2 - 2\pi G\sigma_{\mathrm{b}}|k(r)|. \tag{5}$$

Both these dispersion relations can be linearized to

$$|k(r)| = \frac{|\mathscr{D}||r - r_{\mathrm{res}}|}{2\pi G\sigma_{\mathrm{b}} r_{\mathrm{res}}}, \tag{6}$$

where r_{res} is the radial location of the resonance and

$$\mathscr{D} = \frac{21}{2} J_2 \left(\frac{R_{\mathrm{S}}}{r_{\mathrm{res}}}\right)^2 n^2(r_{\mathrm{res}}) \tag{7}$$

for $m = 1$ resonances (Cuzzi et al., 1984). Since both $\mathscr{D}$ and $r - r_{\mathrm{res}}$ are always positive in the $m = 1$ case, we can combine Eqs. (6) and (7) to write the wavenumber as

$$k(r) = \frac{21 J_2 R_{\mathrm{S}}^2 M_{\mathrm{S}}}{4\pi r_{\mathrm{res}}^6} \cdot \frac{r - r_{\mathrm{res}}}{\sigma_{\mathrm{b}}}. \tag{8}$$

Using standard values for Saturn of $R_{\mathrm{S}} = 60{,}330$ km, $M_{\mathrm{S}} = 5.68 \times 10^{26}$ kg, and $J_2 = 0.01629$ (Jacobson et al., 2006), we can write the wavelength $\lambda \equiv 2\pi/k$ for $m = 1$ resonances in the useful form

$$k(r) = (0.0117\ \mathrm{km}^{-2})(r - r_{\mathrm{res}})\left(\frac{R_{\mathrm{S}}}{r_{\mathrm{res}}}\right)^6 \left(\frac{10\ \mathrm{g\ cm}^{-2}}{\sigma_{\mathrm{b}}}\right). \tag{9}$$

When the background surface density σ_{b} is constant, it is evident from Eq. (9) that $\mathrm{d}k/\mathrm{d}r$ is constant. Most spiral waves in Saturn's rings span a small enough region that this assumption is robust, such that σ_{b} can be obtained by finding the slope of a line fit to $k(r)$, as has been done by several workers with *Cassini* data (Tiscareno et al., 2007; Colwell et al., 2009a; Baillié et al., 2011). Some of the complex waves due to the co-orbital moons Janus and Epimetheus were fit using a different method by Tiscareno et al. (2006). The waves discussed in this work, on the other hand, span large regions of this disk, over which the background surface density varies widely. In this case, as a consequence of the WKB approximation that underlies linear spiral wave theory (Goldreich and Tremaine, 1982; Shu, 1984), we can still use Eq. (9) with the measured wavenumber $k(r)$ at each radial location giving the local surface density $\sigma_{\mathrm{b}}(r)$.

4. Observations

The Iapetus nodal bending wave is visible in *Cassini* ISS images taken during an interval broadly extending from 2008 to 2010, when the solar incidence angle ι was within several degrees of 90° (though it was not noticed until it became very prominent in images taken in spring 2009). The feature is more prominent as ι approaches 90° (equinox), so we concentrate our analysis on two images taken during Orbit 116, with portions of the Sun's disk on both sides of the ring plane. See Table 1 for relevant geometrical parameters. Due to practical constraints on the viewing geometry, these images were taken at a local longitude of 109.3° while the Sun was at a longitude of 224.5°. The difference between the two longitudes is −115.2°, closer to local morning than to local noon or midnight, the latter of which are more optimal for highlighting vertical structure (Fig. 1), yet far enough from local morning that the vertical structure is sufficiently highlighted.

All images were calibrated and converted to values of I/F using the standard Cisscal package v3.6 (Porco et al., 2004). The images were navigated using stars and ring edges as fiducials. We then used SPICE geometry software (Acton, 1996) with NAIF kernels[9] encoding the motions of Saturn, its moons, and the spacecraft, to assign a ring radius (i.e., distance from Saturn center within the ring plane) to each pixel and co-add pixels appropriately to assemble a radial brightness profile for each image. Further conversion could

---

[8] Another reason for the more complex resonance argument for the nodal bending wave is one of d'Alembert's rules (see, e.g., Hamilton, 1994; Murray and Dermott, 1999), which states that the sum of all nodal coefficients in a valid resonance argument must be an even number (in Eq. (3), the coefficients of $\dot{\Omega}'$ and $\dot{\Omega}$ sum to zero, satisfying the rule). For mathematical details of nodal resonances, see Rosen and Lissauer (1988).

[9] Available at `ftp://naif.jpl.nasa.gov`.

Table 1
Observing information for images used in this work.

Image	Orbit	Date/time	Incidence angle[a] (°)	Emission angle[a] (°)	Phase angle (°)	Radial resolution[b]	Azimuthal resolution[b]	Exposure duration[c]
N1560311316	046	2007–163 03:14:24	102.06	125.4	44.1	0.9	0.9	0.5
N1560311433	046	2007–163 03:16:21	102.06	125.0	43.8	0.9	0.9	0.5
N1560311549	046	2007–163 03:18:17	102.06	124.5	43.6	1.0	0.9	0.5
N1628594653	116	2009–222 10:42:04	90.01	94.8	150.0	7.0	45.1	1.0
N1628594713	116	2009–222 10:43:04	90.01	94.8	150.1	7.0	45.1	0.7

[a] Measured from the direction of Saturn's north pole (ring-plane normal), so that 90° denotes edge-on and >90° denotes the southern hemisphere. Note that the Sun's angular size, as seen from Saturn, is 0.06°.

[b] In km/pixel.

[c] In seconds.

be attempted, from simple observed brightness to the ring's optical depth, and from optical depth to surface density. However, these are difficult because of the complex ways in which ring material interacts with light (e.g., Tiscareno et al., 2010b), especially during equinox; furthermore, they are unnecessary because we are interested only in the spatial periodicities of the waves we are examining, and those periodicities can be inferred from the brightness profiles alone since the optical depth and surface density are known to vary with brightness in a relatively simple manner (Cuzzi et al., 1984).

5. Wavelet analysis

A Morlet wavelet transform, which acts as a spatially-resolved Fourier transform for quasi-sinusoidal signals with spatially-varying frequencies, was carried out on each radial brightness profile using techniques described by Tiscareno et al. (2007). In the resulting periodograms, the horizontal axis is the radial coordinate r while the vertical axis is the spatial wavenumber $k = 2\pi/\lambda$ (where λ is the spatial wavelength) and shading indicates the strength of a given frequency at a given radial location.

5.1. Iapetus −1:0 nodal bending wave

The wavelet transform of the Iapetus −1:0 nodal bending wave, as seen in greatest detail on 2009 August 10, is shown in Fig. 5. It is clear that this feature is the −1:0 nodal bending wave, rather than the 1:0 apsidal density wave as claimed by Cuzzi et al. (1981), not only because of the strong dependence of its visibility on the solar incidence angle, but also because Fig. 5 shows the first full wavelength of the outward-propagating wave, as well as much power in the wavelet transform, occuring inward of the Iapetus 1:0 apsidal resonance. It should be noted that the *Voyager* imaging data used by Cuzzi et al. (1981) may have had insufficient spatial resolution to clearly make this distinction, and also that they wrote before Rosen and Lissauer (1988) first worked out the theory of nodal bending waves.

A harmonic signal can be seen in the wavelet transform (Fig. 5) between 121,300 km and 122,200 km, with wavenumbers exactly twice that of the main signal. This is a numerical artifact that arises because the signal is not perfectly sinusoidal (Tiscareno et al., 2007).

As described by Tiscareno et al. (2007), the most accurate way to track the changing wavenumber of a quasi-sinusoidal signal is to analyze the wavelet phase $\bar{\phi}_W(r)$—which essentially measures the respective proximity of local peaks and troughs—at each location, after first zeroing out the wavelet transform for wavenumbers lower than the desired signal (Fig. 6a). The latter is a form of high-pass filter that removes unwanted long-wavelength structure. The wavelet phase $\bar{\phi}_W$ (Fig. 6b) is "unwrapped" to yield a monotonically increasing function of radius (Fig. 6c), and the wavenumber is then calculated as $k = \mathrm{d}\bar{\phi}_W/\mathrm{d}r$ and converted to the local surface density σ_b by means of Eq. (9).

The resulting estimates of local surface density $\sigma_b(r)$ are shown in Fig. 7. The local scatter is due primarily to residual oscillations in $\bar{\phi}_W(r)$ that arise because the signal is not perfectly sinusoidal, as well as gaussian variation in $\bar{\phi}_W(r)$, both of which are amplified by the derivative used to calculate $k(r)$ and then $\sigma_b(r)$. In order to

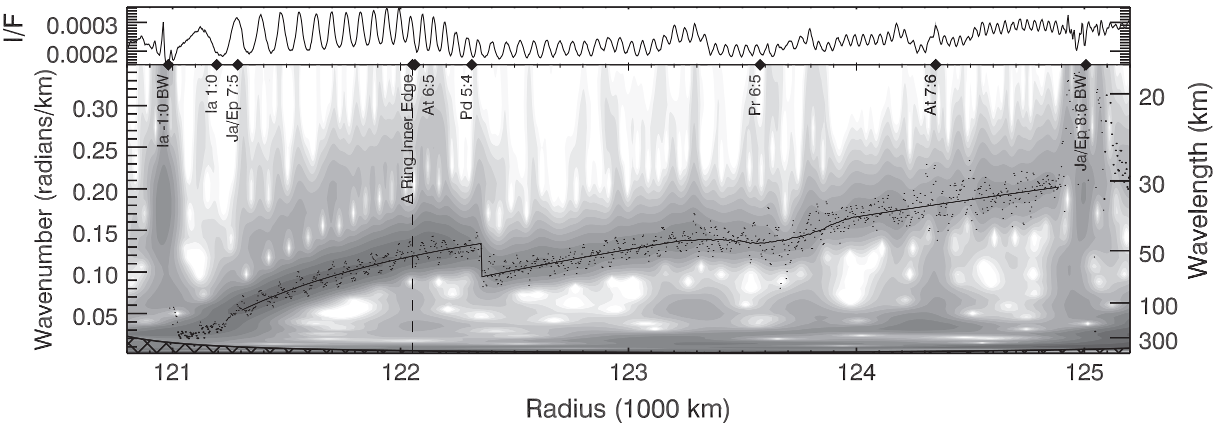

Fig. 5. The upper panel shows the radial brightness profile of the region of interest taken during equinox (from images N1628594653 and N1628594713, taken on 2009 August 10), the same as in the lower panel of Fig. 4. The lower panel shows the Morlet wavelet transform of that brightness profile. Resonances and other features of interest are shown as filled circles on the line between the panels and labeled with text; note the $\sim$200-km radial separation between the locations of the Iapetus −1:0 nodal resonance and the Iapetus 1:0 apsidal resonance. The canonical inner edge of the A ring is also shown as a vertical dashed line. The solid line is a fitted wavenumber profile for the Iapetus −1:0 nodal bending wave, corresponding to the surface density profile shown in Fig. 8. The scattered dots are the raw data from which the fitted profile was derived (see Fig. 7).

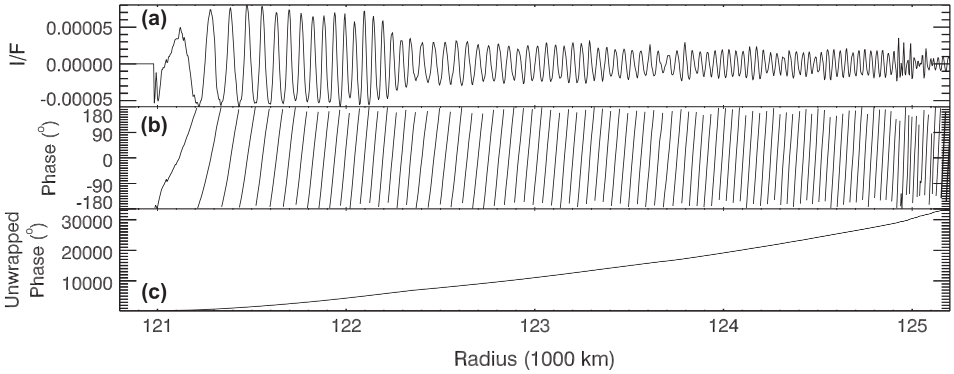

Fig. 6. (a) High-pass filtered (see Section 5.1) radial brightness profile of the region of interest taken during equinox (for unfiltered version, see lower panel of Fig. 4 and upper panel of Fig. 5). (b) Wavelet phase $\bar{\phi}_W(r)$, which is zero near local peaks and 180° near local troughs. (c) Unwrapped wavelet phase, compiled by simply adding to $\bar{\phi}_W(r)$, which constantly increases, another factor of 360° every time it passes through 180°.

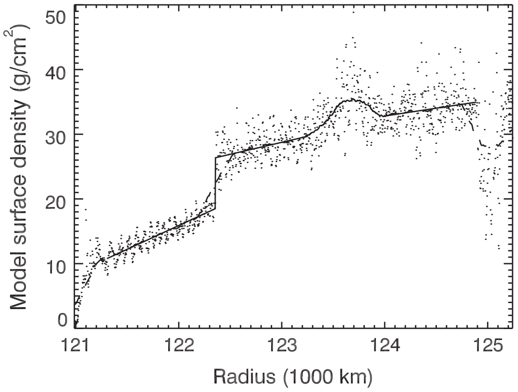

Fig. 7. The scattered dots are the calculated surface density σ_b at each radial location, calculated from Eq. (9) with $k = d\bar{\phi}_W/dr$, where $\bar{\phi}_W(r)$ is plotted in Fig. 6c. The dashed line is the result of a simple low-pass smoothing filter with a boxcar width of 100 elements. The solid line is a more sophisticated model of the surface density profile, derived by taking piecewise linear fits on the intervals [121,300; 122,357] km, [122,357; 123,250] km, and [124,000; 124,890] km, and simply following the boxcar filter on the interval [123,250; 124,000] km. The derived model follows the simple boxcar filter closely at all points except where the latter clearly fails to represent the data, at either end due to the inclusion of non-bending-wave points into the smoothing, and near 122,357 km due to smoothing over the sharp discontinuity.

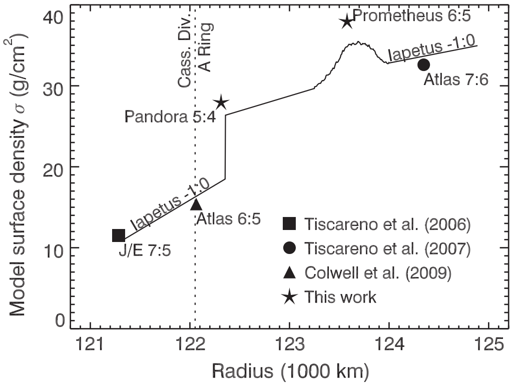

Fig. 8. The solid line denotes our derived surface density profile from the Iapetus −1:0 nodal bending wave (Fig. 7). There is no sharp change in surface density σ_b to correspond with the observed sharp change in optical depth τ at the canonical inner edge of the A ring (vertical dotted line; cf. Fig. 3). Other plotted symbols indicate independent measurements of the surface density from other (spatially smaller) spiral density waves.

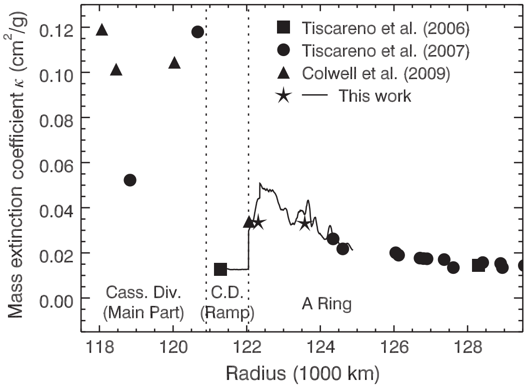

Fig. 9. Mass extinction coefficient $\kappa \equiv \tau/\sigma$, derived from the surface density σ measured for individual spiral density waves and the background optical depth τ at each location (the values of τ are taken from the *Cassini* VIMS stellar occultation plotted in the lower panel of Fig. 3). The mass extinction coefficient appears to be highest in the main part of the Cassini Division, lowest in the Cassini Division Ramp, and to take an intermediate value in the inner-A ring, trending gently lower into the mid-A ring. Overplotted as a solid line is the mass extinction coefficient derived by this work from the Iapetus −1:0 nodal bending wave.

convert these data into a model that can be used for further analysis, smoothing out the scatter while preserving the sharp discontinuity at the Pandora 5:4 resonance location, we fit the data by several piecewise linear fits, as described in Fig. 7. The close correspondence between our derived model and a simple smoothing of the data, except at locations where the latter is clearly deficient, supports our derivation.

Our derived $\sigma_b(r)$ is plotted in Fig. 8 along with independent measurements of σ_b at certain locations as ascertained by means of other spiral density waves[10] (keep in mind that the nodal bending wave has much longer wavelengths and covers much more territory than common spiral waves, as described in Section 3). The agreement gives further support to our derived model. Additionally, the wavenumber $k(r)$ as derived from our model $\sigma_b(r)$ by means of Eq. (9) is overplotted on the wavelet transform in Fig. 5.

---

[10] Surface densities derived from the Pandora 5:4 and Prometheus 6:5 are reported for the first time in this work. Starting with radial brightness scans of images N1560311549 and N1560311316, respectively, we simply found by eye the value of σ_0 that gave the best match to the slope of the wave's wavelet signature in radius-wavenumber space (see Eq. (6), which applies for all values of m), as irregular waveforms (see Fig. 10) preclude use of the more sophisticated method developed by Tiscareno et al. (2007). We obtained $\sigma_0 = 28 \pm 5$ g cm^{-2} from the Pandora 5:4 wave originating at r = 122,313 km, and $\sigma_0 = 38 \pm 5$ g cm^{-2} from the Prometheus 6:5 wave originating at r = 123,578 km.

The mass extinction coefficient $\kappa \equiv \tau/\sigma$ measures the ring's light-blocking ability per unit surface density. Higher values of κ, indicating more light-blocking surface area for a given surface density, are most simply achieved by breaking the mass into smaller particles. Contrariwise, lower values of κ are most simply achieved by concentrating the mass into large particles or clumps. The mass extinction coefficient as derived by this work is placed in the context of previous observations in Fig. 9 and clarifies the situation considerably. It is now evident that the Cassini Division Ramp is a region of particularly low κ, as much as 10× lower than in the main part of the Cassini Division, while values of κ in the inner-A ring are intermediate and trend gently lower into the mid-A ring.

5.2. Pandora 5:4 density wave

While it has been commonly repeated that the Pandora 5:4 density wave has the longest train of any in the A ring (e.g., Colwell et al., 2009b), in fact it can be seen in Fig. 10 that only the inner ~100 km of the oscillations have significant power in the $k \propto (r - r_{\mathrm{res}})$ pattern that is characteristic of propagating density waves. The remaining several thousand km of high-frequency structure does not show any evidence of frequencies related to the Pandora 5:4 density wave. Furthermore, given the surface density model shown in Fig. 10, the wavelength of the Pandora 5:4 wave would reach values as small as tens of meters, if indeed it propagated all the way to the outer edge of the high-frequency region at 125,250 km.

Rather, it is likely that the Pandora 5:4 wave merely serves as the inner boundary of a region marked by high spatial frequencies (as well as high surface densities) that are likely due to viscous overstability (Thomson et al., 2007; Colwell et al., 2007; Schmidt et al., 2009) and perhaps other processes. Whether this spatial arrangement occurs through causality or simply by coincidence is not clear. Because Lindblad resonances transfer negative angular momentum into the disk, it should not be possible for the Pandora 5:4 wave to actively maintain the mass shelf at its location (as, for example, the Mimas 2:1 and Janus/Epimetheus 7:6 resonances respectively maintain the *outer* edges of the B and A rings). On the other hand, the strong oscillations of the Pandora 5:4 density wave may play a role in triggering the viscous overstability in a region that, for other reasons, is susceptible to it.

6. Discussion

The lack of a sharp jump in surface density at the inner edge of the A ring (Fig. 8) is surprising and difficult to explain. What could drive the observed sharp jump in optical depth, if not the surface density? In other words, what could drive a sharp jump in the mass extinction coefficient κ at that location (Fig. 9)?

One way for the optical depth to change sharply with only a modest trend in surface density is if the surface density were to pass through a threshold value at which self-gravity wakes (SGWs) "turned on." Indeed, SGWs do exist throughout the inner A ring but not in the Cassini Division Ramp (Nicholson and Hedman, 2010). SGWs, which are pervasive clumps due to a gravitational instability that is not strong enough to run completely to accretion (e.g., Schmidt et al., 2009) can indeed have a sudden onset as well as a strong effect on the mass extinction coefficient (Daisaka et al., 2001; Tiscareno et al., 2010b). However, the observed effect is in the wrong direction, as the onset of SGWs would be triggered by rising surface density and would *decrease* the optical depth for a given surface density. Therefore, SGWs cannot answer the puzzle posed by our findings.

The most straightforward interpretation of these observations is that the inner-A ring is composed of smaller particles (on average) than the Cassini Division Ramp, while the main part of the Cassini Division is composed of still smaller particles. Why the Cassini Division Ramp would have such large particles, and why there would be a sharp boundary in the particle-size distribution, is not clear. Ballistic transport (Durisen et al., 1992) may conceivably operate to sharpen an edge in optical depth without an edge in surface density, or particles of different sizes may migrate radially at different rates in such a way as to give rise to a separation, but further study is needed to determine whether that is possible. Another possibility is that the Cassini Division Ramp was the site of an impact that seeded that region with larger particles that have not yet come to collisional equilibrium, but this too requires further study to evaluate its plausibility. Further study is also needed to determine whether the varying particle-size distributions suggested in this paragraph can be reconciled with the "excess variance" patterns measured by stellar occultations (Showalter and Nicholson, 1990; Colwell et al., 2011) and with the multi-wavelength diffraction data from *Cassini* radio occultations (e.g., Cuzzi et al., 2009).

Finally, our findings raise the question of whether the Cassini Division Ramp would more usefully be reckoned as the innermost part of the A ring, rather than as the outermost part of the Cassini Division (similarly, whether the C ring Ramp might have more in common with the inner-B ring than with the rest of the C ring). A possible compositional affinity was previously mentioned in Section 2. The densest part of the A ring is the apparently "chaotic region" from 122,350 km to ~125,000 km, which is likely characterized by viscous overstability. The inner edge of that region is a precipitous drop in both optical depth and surface density at the

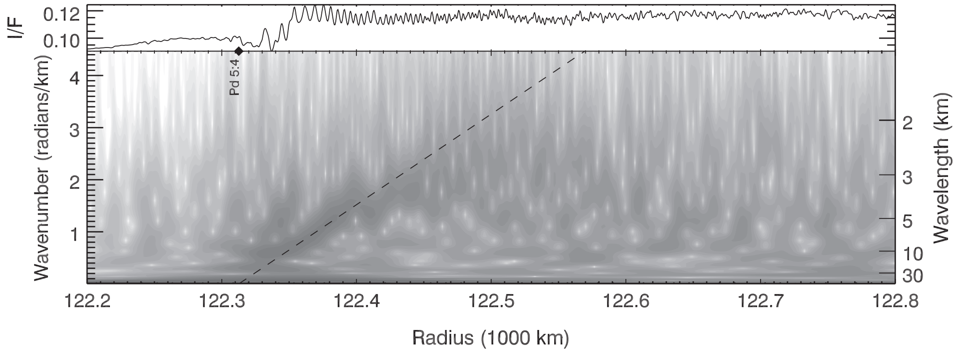

Fig. 10. The upper panel shows a radial brightness profile of the region surrounding the Pandora 5:4 density wave, taken with its normal appearance (the Sun was 12° out of the ring plane; see Table 1). The images are N1560311433 and N1560311549, taken on 2007 June 12. As in Fig. 5, the lower panel shows the Morlet wavelet transform of that brightness profile. The location of the Pandora 5:4 Lindblad resonance is marked at 122,313 km, and the dashed line shows the expected wavenumber trace for $\sigma_b = 28\ \mathrm{g\ cm^{-2}}$ (Eq. (9)), which fits the data.

location of the Pandora 5:4 resonance (122,313 km), but the boundaries are not sharp.[11] Further inward (see Figs. 3 and 8) is a 250-km "doorstep" region of intermediate optical depth, whose inner boundary at the canonical inner edge of the A ring (122,050 km) is now revealed as a sharp edge in optical depth but not in surface density (thus, as a sharp edge in mass extinction coefficient κ, most easily explained by means of particle properties). The surface density decreases steadily inward from the Pandora resonance to the inner reaches of the Ramp. Perhaps the real inner edge of the A ring complex should be reckoned at 120,900 km, where the Cassini Division's "triple band" feature gives way to the first risings of the Ramp.

However, no change in nomenclature will solve the primary question raised by this work: What is the nature of the changes in ring properties at 122,050 km, the canonical inner edge of the A ring, and why do they occur?

Acknowledgments

We thank Jeff Cuzzi and Peter Goldreich for helpful conversations, and Jürgen Schmidt and Larry Esposito for improvements to the manuscript. We thank the Cassini Project and the Cassini Imaging Team. M.S.T. acknowledges funding from the NASA Cassini Data Analysis program (NNX08AQ72G and NNX10AG67G) and the Cassini Project.

References

Acton, C.H., 1996. Ancillary data services of NASA's Navigation and Ancillary Information Facility. Planet. Space Sci. 44, 65–70.

Baillié, K., Colwell, J.E., Lissauer, J.J., Esposito, L.W., Sremčević, M., 2011. Waves in Cassini UVIS stellar occultations. 2. The C ring. Icarus 216, 292–308.

Colwell, J.E., Esposito, L.W., Sremčević, M., Stewart, G.R., McClintock, W.E., 2007. Self-gravity wakes and radial structure of Saturn's B ring. Icarus 190, 127–144.

Colwell, J.E., Cooney, J.H., Esposito, L.W., Sremčević, M., 2009a. Density waves in Cassini UVIS stellar occultations. 1. The Cassini Division. Icarus 200, 574–580.

Colwell, J.E., Nicholson, P.D., Tiscareno, M.S., Murray, C.D., French, R.G., Marouf, E.A., 2009b. The structure of Saturn's rings. In: Dougherty, M., Esposito, L., Krimigis, S.M. (Eds.), Saturn from Cassini–Huygens. Springer-Verlag, Dordrecht, pp. 375–412.

Colwell, J.E., Cooney, J.H., Esposito, L.W., 2011. Particle size variations in Saturn's rings from occultation statistics. AAS Div. Planet. Sci. Meet. 43, 1282 (abstracts).

Cuzzi, J.N. et al., 1984. Saturn's rings: Properties and processes. In: Greenberg, R., Brahic, A. (Eds.), Planetary Rings. Univ. Arizona Press, Tucson, pp. 73–199.

Cuzzi, J. et al., 2009. Ring particle composition and size distribution. In: Dougherty, M., Esposito, L., Krimigis, S.M. (Eds.), Saturn from Cassini-Huygens. Springer-Verlag, Dordrecht, pp. 459–509.

Cuzzi, J.N., Lissauer, J.J., Shu, F.H., 1981. Density waves in Saturn's rings. Nature 292, 703–707.

Daisaka, H., Tanaka, H., Ida, S., 2001. Viscosity in a dense planetary ring with self-gravitating particles. Icarus 154, 296–312.

Durisen, R.H., Bode, P.W., Cuzzi, J.N., Cederbloom, S.E., Murphy, B.W., 1992. Ballistic transport in planetary ring systems due to particle erosion mechanisms II. Theoretical models for Saturn's A- and B-ring inner edges. Icarus 100, 364–393.

Esposito, L.W., O'Callaghan, M., West, R.A., 1983. The structure of Saturn's rings: Implications from the Voyager stellar occultation. Icarus 56, 439–452.

French, R.G., Nicholson, P.D., Cooke, M.L., Elliot, J.L., Matthews, K., Perkovic, O., Tollestrup, E., Harvey, P., Chanover, N.J., Clark, M.A., Dunham, E.W., Forrest, W., Harrington, J., Pipher, J., Brahic, A., Grenier, I., Roques, F., Arndt, M., 1993. Geometry of the Saturn system from the 3 July 1989 occultation of 28 SGR and Voyager observations. Icarus 103, 163–214.

Goldreich, P., Tremaine, S., 1978. The formation of the Cassini Division in Saturn's rings. Icarus 34, 240–253.

Goldreich, P., Tremaine, S., 1979. The excitation of density waves at the Lindblad and corotation resonances by an external potential. Astrophys. J. 233, 857–871.

Goldreich, P., Tremaine, S., 1980. Disk-satellite interactions. Astrophys. J. 241, 425–441.

Goldreich, P., Tremaine, S., 1982. The dynamics of planetary rings. Ann. Rev. Astron. Astrophys. 20, 249–283.

Gresh, D.L., Rosen, P.A., Tyler, G.L., Lissauer, J.J., 1986. An analysis of bending waves in Saturn's rings using Voyager radio occultation data. Icarus 68, 481–502.

Hamilton, D.P., 1994. A comparison of Lorentz, planetary gravitational, and satellite gravitational resonances. Icarus 109, 221–240.

Hedman, M.M., Burns, J.A., Evans, M.W., Tiscareno, M.S., Porco, C.C., 2011. Saturn's curiously corrugated C ring. Science 332, 708–711.

Hedman, M.M., Nicholson, P.D., Salo, H., 2012. Probing periodic patterns in Saturn's inner A ring with Cassini-VIMS. AAS Div. Planet. Sci. Meet. 44, 414.05 (abstracts).

Hedman, M.M., Nicholson, P.D., Cuzzi, J.N., Clark, R.N., Filacchione, G., Capaccioni, F., Ciarniello, M., 2013. Connections between spectra and structure in Saturn's main rings based on Cassini VIMS data. Icarus 223, 105–130.

Jacobson, R.A. et al., 2006. The gravity field of the saturnian system from satellite observations and spacecraft tracking data. Astron. J. 132, 2520–2526.

Lainey, V. et al., 2012b. Strong tidal dissipation in Saturn and constraints on Enceladus' thermal state from astrometry. Astrophys. J. 752, 14.

Lainey, V., Charnoz, S., Reboussin, L., Noyelles, B., Baillié, K., 2012a. The Cassini Division and Mimas' eccentricity: A common history. AAS Div. Planet. Sci. Meet. 44, 414.08 (abstracts).

Murray, C.D., Dermott, S.F., 1999. Solar System Dynamics. Cambridge Univ. Press, Cambridge.

Nicholson, P.D., Hedman, M.M., 2010. Self-gravity wake parameters in Saturn's A and B rings. Icarus 206, 410–423.

Nicholson, P.D., Porco, C.C., 1988. A new constraint on Saturn's zonal gravity harmonics from Voyager observations of an eccentric ringlet. J. Geophys. Res. 93, 10209–10224.

Porco, C.C. et al., 2004. Cassini imaging science: Instrument characteristics and anticipated scientific investigations at Saturn. Space Sci. Rev. 115, 363–497.

Porco, C., Nicholson, P.D., Borderies, N., Danielson, G.E., Goldreich, P., Holberg, J.B., Lane, A.L., 1984. The eccentric saturnian ringlets at $1.29R_S$ and $1.45R_S$. Icarus 60, 1–16.

Rein, H., Latter, H., 2013. Large-scale N-body simulations of the viscous overstability in Saturn's rings. Mon. Not. Roy. Astron. Soc., in press. arXiv:1210.3358.

Robbins, S.J., Stewart, G.R., Lewis, M.C., Colwell, J.E., Sremčević, M., 2010. Estimating the masses of Saturn's A and B rings from high-optical depth N-body simulations and stellar occultations. Icarus 206, 431–445.

Rosen, P.A., Lissauer, J.J., 1988. The Titan -1:0 nodal bending wave in Saturn's Ring C. Science 241, 690–694.

Rosen, P.A., Tyler, G.L., Marouf, E.A., 1991. Resonance structures in Saturn's rings probed by radio occultation I. Methods and examples. Icarus 93, 3–24.

Schmidt, J., Ohtsuki, K., Rappaport, N., Salo, H., Spahn, F., 2009. Dynamics of Saturn's dense rings. In: Dougherty, M., Esposito, L., Krimigis, S.M. (Eds.), Saturn from Cassini–Huygens. Springer-Verlag, Dordrecht, pp. 413–458.

Showalter, M.R., Nicholson, P.D., 1990. Saturn's rings through a microscope: Particle size constraints from the Voyager PPS scan. Icarus 87, 285–306.

Shu, F.H., 1984. Waves in planetary rings. In: Greenberg, R., Brahic, A. (Eds.), Planetary Rings. Univ. Arizona Press, Tucson, pp. 513–561.

Shu, F.H., Cuzzi, J.N., Lissauer, J.J., 1983. Bending waves in Saturn's rings. Icarus 53, 185–206.

Spitale, J.N., Porco, C.C., 2010. Detection of free unstable modes and massive bodies in Saturn's outer B ring. Astron. J. 140, 1747–1757.

Thomson, F.S., Marouf, E.A., Tyler, G.L., French, R.G., Rappaport, N.J., 2007. Periodic microstructure in Saturn's rings A and B. Geophys. Res. Lett. 34, L24203.

Tiscareno, M.S. et al., 2010a. Physical characteristics and non-keplerian orbital motion of "propeller" moons embedded in Saturn's rings. Astrophys. J. 718, L92–L96.

Tiscareno, M.S. et al., 2010b. An analytic parameterization of self-gravity wakes in Saturn's rings. Astron. J. 139, 492–503.

Tiscareno, M.S., 2013. Planetary rings. In: Oswalt, T.D., French, L., Kalas, P. (Eds.), Planets, Stars, and Stellar Systems, Solar and Stellar Planetary Systems, vol. 3. Springer, Dordrecht., in press. arXiv:1112.3305.

Tiscareno, M.S., Nicholson, P.D., Burns, J.A., Hedman, M.M., Porco, C.C., 2006. Unravelling temporal variability in Saturn's spiral density waves: Results and predictions. Astrophys. J. 651, L65–L68.

Tiscareno, M.S., Burns, J.A., Nicholson, P.D., Hedman, M.M., Porco, C.C., 2007. Cassini imaging of Saturn's rings II. A wavelet technique for analysis of density waves and other radial structure in the rings. Icarus 189, 14–34.

Tiscareno, M.S. et al., 2013. Observations of ejecta clouds produced by impacts onto Saturn's rings. Science, submitted for publication.

Tyler, G.L., Marouf, E.A., Simpson, R.A., Zebker, H.A., Eshleman, V.R., 1983. The microwave opacity of Saturn's rings at wavelengths of 3.6 and 13 cm from Voyager 1 radio occultation. Icarus 54, 160–188.

Weiss, J.W., Porco, C.C., Tiscareno, M.S., 2009. Ring edge waves and the masses of nearby satellites. Astron. J. 138, 272–286.

---

[11] In fact, the lack of a reflected wave propagating inward from this location (Fig. 5) indicates that the transition in surface density is not much sharper than the wavelength at that location, ~50 km.